Journal of Molecular Structure 1235 (2021) 130266

Contents lists available at ScienceDirect

Journal of Molecular Structure

journal homepage: www.elsevier.com/locate/molstr

# Experimental and *in silico* studies of dichloro-*tetrakis*(1H-pyrazole)-cobalt(II): Structural description, photoluminescent behavior and molecular docking

Amani Direm[a,*], Brahim El Bali[b], Koray Sayin[c], Mohammed S.M. Abdelbaky[d], Santiago García-Granda[d]

[a] *Laboratory of Structures, Properties and Interatomic Interactions LASPI2A, Department of Matter Sciences, Faculty of Sciences and Technology, Abbes Laghrour University Khenchela, 40.000 Algeria*
[b] *Independent scientist, Oujda, Morocco*
[c] *Department of Chemistry, Faculty of Science, Cumhuriyet University 58140 Sivas – Turkey*
[d] *Departamento de Química Física y Analítica, Universidad de Oviedo-CINN, 33006 Oviedo, Spain*

ARTICLE INFO

*Article history:*
Received 20 November 2020
Revised 20 February 2021
Accepted 5 March 2021
Available online 10 March 2021

*Keywords:*
Pyrazole complex
Topological analysis
Hirshfeld surface analysis
Photoluminescence
*In silico* study
Molecular docking

ABSTRACT

A novel pyrazole-based Co(II) complex, namely dichloro-tetrakis(1H-pyrazole)-cobalt(II), was synthesized and characterized. Its X-ray crystal structure showed that it crystallizes in the monoclinic *C*2/*c* space group with discrete $[CoPz_4Cl_2]$ units held together *via* intra- and intermolecular hydrogen bonds. The non-covalent interactions were explicitly analyzed by means of the topological and *Hirshfeld* surface analyses, revealing the presence of 0-periodic binodal 1,6-connected **1,6M7–1** and 14-connected uninodal **bcu–x** topologies built up through N—H…Cl and C—H…Cl hydrogen-bonding networks in addition to weak non-classical H…H, N–H…C, C–H…N, N—H…$\pi$, $\pi$…*lp*/*lp*…$\pi$ and *lp*…*lp* interactions. Additionally, interactions energy and energy frameworks analyses were performed in order to compute the total energies of the possible intermolecular interactions. The empty space in the crystal lattice was analyzed using *void mapping* which lead to the presence of small cavities. The structure was furthermore optimized showing a very good agreement with the experimental results, the molecular electrostatic potential (MEP) maps were obtained with their active regions and the non-linear optical properties estimated. Additionally, the optical properties of the title complex were investigated at room temperature using optical UV-visible absorption and photoluminescence spectroscopy, exhibiting $\pi \rightarrow \pi^*$, n $\rightarrow \pi^*$, $d \rightarrow d$ and ligand-field transitions which result in a large variety of emission bands predominant by a bright red photoluminescence. An *in silico* study was carried out and the binding ability of the title complex with *Staphylococcus aureus* tyrosyl-tRNA synthetase and *Pyrococcus kodakaraensis* aspartyl-tRNA synthetase was evaluated displaying a good inhibition activity towards the last one.



## 1. Introduction

Heterocyclic compounds containing nitrogen, oxygen and sulfur, and their metal complexes are biologically active materials toward bacteria, fungi and viruses [1–5]. Especially, pyrazole-based ones, referred to hereafter as Pz, are applied in the pharmaceutical and agrochemical fields [6]. The pyrazolate ligand can exhibit three coordination modes. It can act as a monodentate (pyrazole-N) and exo-bidentate (pyrazole N,N) or an endo-bidentate ligand [7,8]. In most cases, the pyrazolate ligand coordinates in an exo-bidentate fashion, thus linking two metal centres that may be identical or different. Recent studies have described the catalytic activity of pyrazolate complexes [8,9] under mild conditions, thus encouraging the exploration of these ligands.

In fact, since the first review of pyrazole-derived ligands appeared in 1972 [10], the coordination chemistry of Pz and its derivatives has strongly evolved over the last two decades [11]. Pz derivatives have many other applications such as analgesic [12], antibacterial [13], anti-hyperglycemic [14], anti-inflammatory [15], antipyretic [16], hypoglycaemic [17] and sedative hypnotic activities [18]. The ones such as *celecoxib, rimonabant, fomepizole* and *sildenafil* were established as selective drugs [19]. In fact, *celecoxib* demonstrated anti-inflammatory effect and inhibited cox-2 [20], while *rimonabant* is a cannabixiod receptor and is used for obesity treatment. *Bindenafil* and *fomepizole* inhibit phosphodiesterase

* Corresponding author.
*E-mail address:* amani_direm@yahoo.fr (A. Direm).

https://doi.org/10.1016/j.molstruc.2021.130266
0022-2860/

and alcohol dehydrogenase, respectively [21]. Some Pz derivatives also have nonnucleoside HIV-1 reverse transcriptase inhibitory activities [21–24]. The transition metal Pz complexes are also active metallobiomolecules. The acid and amido derivatives of Pz compounds are important heterocycles for the synthesis of metallobiomolecules [25]. Copper- and cobalt-Pz complexes showed excellent antibacterial and antifungal activities [26–28]. Especially, Cu-complexes were synthesized to screen the biological activities and some of them were active both *in vivo* and *in vitro* [20,28].

Hydrogen bonding in coordination compounds is an important issue as it can often explain the formation and/or stability of an unusual coordination compound. The matter is well known in general and has been reviewed a few times [29]. A recent review on Pz and hydrogen bonds is available [30]. However, when coordinating counter anions like halides were used, many quite stable compounds of formula $[M(Hpz)_4X_2]$ were found for several transition metal ions with pyrazoles and substituted-pyrazoles [30–35]. Intramolecular hydrogen bonding was found in such cases and discussed in some details, so far mainly for nickel(II) [31,36].

In this report, we explore the synthesis, crystal structure and intermolecular interactions exhibited by dichloro-*tetrakis*(1H-pyrazole)-cobalt(II) *via* topological and *Hirshfeld* surface analyses. Additionally, we report herein the optical and photoluminescence properties of the mentioned material which exhibited a strong red emission. Furthermore, the quantum chemical calculations of the title complex were performed at HF/6–31+G(d)(LANL2DZ) and B3LYP/6–31+G(d)(LANL2DZ) levels in vacuum. The best calculation level is determined as B3LYP/6–31+G(d)(LANL2DZ). The contour diagrams of single occupied molecular orbital (SOMO) and the lowest unoccupied molecular orbital (LUMO) were calculated and examined in detail. Additionally, the electrostatic potential (ESP) charges were calculated to obtain the molecular electrostatic potential (MEP) map. The non-linear optical (NLO) properties were theoretically investigated against urea which is mainly used as a reference substance in the investigations of NLO properties. In this analysis, some quantum chemical parameters were calculated and examined categorically. Moreover, we carried out an *in silico* study in order to evaluate the binding effect of the Co(II) complex towards *Staphylococcus aureus* tyrosyl-tRNA synthetase and *Pyrococcus kodakaraensis* aspartyl-tRNA synthetase.

## 2. Materials and methods

### 2.1. Synthesis

To equimolar quantities of pyrazole (0.136 g, 2 mmol) and $CoCl_2$ (0.260 g, 2 mmol), separately dissolved in a mixture of methanol (10 mL) and water (10 mL) and stirred together at 60 °C for one hour, 5 mL of hydrochloric acid was added drop wise. The resulting solution was then filtered and left at room temperature for several days leading to pinkish-purple block-like crystals of dichloro-*tetrakis*(1H-pyrazole)-cobalt(II) (**1**).

### 2.2. Single-crystal X-ray diffraction

Single-crystal X-ray diffraction data collection for the title complex was performed on an Agilent Xcalibur Gemini S single-crystal diffractometer, using MoK$\alpha$ radiation ($\lambda$ = 0.71073 Å) at room temperature. The crystal structure was solved by direct methods using *SIR2014* [37] and refined by full-matrix least-squares methods against $F^2$ using *SHELXL2014* [38], implemented in the *WinGX* software package [39]. All non-H atoms were anisotropically refined, while H atoms were obtained from the difference Fourier maps and refined riding on their parent atoms with fixed isotropic displacement parameters. The crystallographic calculations were carried out using the following programs: CrysAlis CCD for data collection, CrysAlis RED for cell refinement and data reduction [40]. Diamond [41] was used for molecular graphics. Full structural details might be found in the CIF deposited at the Cambridge Crystallographic Data centre, CCDC No 2032295. These data can be obtained free of charge via http://www.ccdc.cam.ac.uk/conts/retrieving.html, or from the CCDC, 12 Union Road, Cambridge, CB2 1EZ, UK: fax: (+44) 01223–336–033; e-mail: deposit@ccdc.cam.ac.

### 2.3. Theoretical calculations

Interest in computational chemistry has been increased in the recent years [42–44]. Quantum chemical analyses of the title compound were performed by using HF and B3LYP methods with 6–31+G(d)(LANL2DZ) mix basis set in vacuum. The optimized structure and geometric parameters were obtained from these calculation results and compared with the experimental ones. Quantum chemical calculations were performed by GaussView 5.0.9 [45] and Gaussian 09 AS64L-G09RevD.01 [46] programs. Hartree-Fock (HF) and Becke-3-LeeYangParr (B3LYP) methods were used with mix basis set, LANL2DZ was used for metal atoms and 6–31+G(d) was used for the other atoms in the complex. Additionally, urea was optimized using the same level of theory. Furthermore, quantum chemical descriptors were calculated by using Eqs. (1) – (9).

$$I = -E_{HOMO} \tag{1}$$

$$A = -E_{LUMO} \tag{2}$$

$$E_{GAP} = E_{LUMO} - E_{HOMO} \tag{3}$$

$$\eta = \frac{I - A}{2} = \frac{E_{LUMO} - E_{HOMO}}{2} \tag{4}$$

$$\sigma = \frac{1}{\eta} \tag{5}$$

$$\sigma_O = \frac{1}{E_{GAP}} \tag{6}$$

$$\chi = \frac{|I + A|}{2} = \frac{|-E_{HOMO} - E_{LUMO}|}{2} \tag{7}$$

$$CP = -\chi \tag{8}$$

$$\Delta N_{Max} = -\frac{CP}{\eta} \tag{9}$$

### 2.4. Physical measurements

#### 2.4.1. UV spectroscopy

The optical absorption spectrum of the studied compound was measured at room temperature using a conventional UV–vis absorption spectrometer (Shimadzu UV 3101).

#### 2.4.2. Photoluminescence

Solid photoluminescence spectra were measured using a time-resolved *Edimbugh* Instruments FLSP920 spectrofluorimeter with a Red-PMT detector and a Xenon bulb as excitation source.

### 2.5. Molecular docking

Molecular docking calculations were done against *Staphylococcus aureus* tyrosyl-tRNA synthetase and *Pyrococcus kodakaraensis* aspartyl-tRNA synthetase by using Maestro 12.2 program [47-52]. The related proteins were selected from protein data bank web tool as **1JIL** [53] and **1B8A** [54], respectively.

**Table 1**
Crystallographic data for (1).

| *Compound* | $CoPz_4Cl_2$ |
|---|---|
| *Systematic name* | dichloro-*tetrakis*(1H-pyrazole)-cobalt(II) |
| *CCDC No* | 2032295 |
| *Empirical formula* | $C_{12}H_{16}Cl_2CoN_8$ |
| *Formula weight/g·mol$^{-1}$* | 402.16 |
| *Temperature/K* | 293(2) |
| *Wavelength/Å* | 0.71073 |
| *Crystal system* | Monoclinic |
| *Space group* | C2/c |
| *Unit cell dimensions* | |
| *a (Å)* | 13.6170(1) |
| *b (Å)* | 9.2934(5) |
| *c (Å)* | 14.9550(1) |
| *β (°)* | 117.920(1) |
| *Cell volume/Å$^3$* | 1672.2(3) |
| *Z* | 4 |
| *Calc. Density/g·cm$^{-3}$* | 1.597 |
| *Absorption coefficient/mm$^{-1}$* | 1.36 |
| *F(000)* | 820 |
| *Crystal size (mm$^3$)* | 0.25 × 0.15 × 0.15 |
| *Theta range for data collection/°* | 3.4 to 31.4 |
| *Index ranges* | $-19 \le h \le 19$, $-13 \le k \le 12$, $-21 \le l \le 21$ |
| *Reflections collected* | |
| *Independent reflections* | 9782<br>2744 [R(int) = 0.034] |
| *Completeness to $\theta_{max}$* | 98% |
| *Absorption correction* | Refined (XABS2) |
| *Max. and min. transmission* | 0.816 and 0.783 |
| *Refinement method* | Full-matrix least-squares on $F^2$ |
| *Data / restraints / parameters* | 2744 / 12 / 106 |
| *Goodness-of-fit on $F^2$* | 1.04 |
| *Final R indices [I>2sigma(I)]* | $R_1 = 0.0424$, $wR_2 = 0.0952$ |
| *R indices (all data)* | $R_1 = 0.0634$, $wR_2 = 0.1057$ |
| *Largest diff. peak and hole/e·Å$^{-3}$* | 0.36 and −0.30 |

**Table 2**
Selected experimental and calculated geometric parameters in (**1**) (Å, °).

| Bond distances | Experimental | Calculated HF Method | B3LYP Method |
|---|---|---|---|
| Co1—N3 | 2.1052(17) | 1.860 | 1.997 |
| Co1—N1 | 2.1253(18) | 1.860 | 1.997 |
| Co1—Cl1 | 2.5700(6) | 2.150 | 2.759 |
| N3—C6 | 1.323(3) | 1.402 | 1.338 |
| N3—N4 | 1.337(3) | 1.392 | 1.348 |
| N1—N2 | 1.334(3) | 1.392 | 1.348 |
| N1—C3 | 1.337(3) | 1.402 | 1.338 |
| N2—C1 | 1.362(4) | 1.392 | 1.349 |
| N4—C4 | 1.333(3) | 1.392 | 1.349 |
| C3—C2 | 1.366(4) | 1.435 | 1.408 |
| C6—C5 | 1.380(3) | 1.435 | 1.408 |
| C1—C2 | 1.355(5) | 1.402 | 1.389 |
| C5—C4 | 1.357(4) | 1.402 | 1.389 |
| Bond angles | | | |
| N3—Co1—N3$^i$ | 180 | 180.00 | 179.99 |
| N3—Co1—N1 | 87.51(7) | 90.00 | 90.23 |
| N3$^i$ —Co1—N1$^i$ | 87.51(7) | 90.00 | 90.23 |
| N3$^i$—Co1—N1 | 92.49(7) | 90.00 | 89.77 |
| N3—Co1—N1$^i$ | 92.49(7) | 89.99 | 89.77 |
| N1—Co1—N1$^i$ | 180 | 180.00 | 179.99 |
| N3—Co1—Cl1 | 89.57(5) | 90.00 | 91.21 |
| N3$^i$—Co1—Cl1 | 90.43(5) | 90.00 | 88.79 |
| N3$^i$—Co1—Cl1$^i$ | 89.57(5) | 89.99 | 91.20 |
| N3—Co1—Cl1$^i$ | 90.43(5) | 90.00 | 88.80 |
| N1—Co1—Cl1 | 90.96(5) | 89.99 | 91.18 |
| N1$^i$ —Co1—Cl1$^i$ | 90.96(5) | 90.00 | 91.20 |
| N1$^i$—Co1—Cl1 | 89.04(5) | 90.00 | 88.81 |
| N1—Co1—Cl1$^i$ | 89.04(5) | 90.00 | 88.81 |
| Cl1—Co1—Cl1$^i$ | 180 | 180.00 | 179.99 |

Symmetry code (*i*): $-x + 3/2$, $-y + 3/2$, $-z + 1$.

**Table 3**
Hydrogen-bond geometry in the crystal structure of (**1**) (Å, °).

| D—H•••A | D—H | H•••A | D•••A | D—H•••A |
|---|---|---|---|---|
| N2—H2N•••Cl1$^{ii}$ | 0.86 | 3.05 | 3.739 (3) | 139 |
| N4—H4N•••Cl1 | 0.86 | 2.53 | 3.138 (2) | 129 |
| C3—H3•••Cl1 | 0.93 | 2.74 | 3.324 (2) | 121 |

Symmetry code (*ii*): $x + 1/2$, $y - 1/2$, $z$.

## 3. Results and discussion

### 3.1. Structural study

#### 3.1.1. Crystal structure description

The detailed crystallographic data and the structure refinement parameters are collected in Table 1. Selected bond distances and angles for (**1**) are given in Table 2, while Table 3 records the hydrogen-bonding networks. Fig. 1a depicts the asymmetric unit cell, with the numbering of the atoms in (**1**), which contains 12 non hydrogen atoms, including one $Co^{2+}$, one $Cl^-$ and two pyrazole "Pz" groups ($C_3H_3N_2H$).

It is worth to be noted that the crystal structure of (**1**) was early solved by Malecki [55] however it was never discussed and fully studied. (**1**) is isostructural to its isoformular Mn (**2**), Ni (**3**) and Cu (**4**) compounds [56–68]. They all crystallize in the monoclinic space group C2/c, with the divalent 3*d* ion ($M^{2+}$) ion occupying an inversion center and their 3D framework is built upon discrete $[MPz_4Cl_2]$ units as shown in Fig. 1b.

The four coordinated Pz ligands are arranged about the $Co^{2+}$ center in a square-planar configuration with the two chloride ions occupying the apical positions, according to a $d^2sp^3$ hybridation of the $Co^{2+}$ ($d^7$) ion in a distorted octahedral coordination scheme at an average distance of 2.15 Å (Fig. 1b, Table 2). The $d_{Co-N}$ distances range between 2.1052(17) and 2.1253(18) Å, typical of M(II)–N distances (av. 2.01045 Å [66] and 2.008 Å [67]) in (**1**). The M(II)–Cl bonds appear to be slightly longer, 2.5700(6) Å, which might originate from the lone-pair electrons on $Cl^-$ and the hydrogen bonding between the $Cl^-$ ions and N–H groups of two Pz ligands [69]. It is however shorter than such bonds in the Cu homologous complex we previously reported; 2.8226(4) Å [66].

A bibliographical survey showed that twelve structures with $Co^{2+}$-containing Pz ligands have been reported in the literature. The most common coordination for Co(II) in these structures is tetrahedral, except in four cases, where the coordination is octahedral [70–73]. The Co–N bond distances in (**1**) are similar to those found in these four structures.

According to the formula $\Delta_{oct} = 1/6^*\Sigma[(d_i\text{-}d_m)/d_m]^2$ [74,75], the bond-length distortion for the $Co^{2+}$ octahedron is of $1.03•10^{-2}$, which indicates slight distortion, with N1–Co–N1$^i$ and N3–Co–N3$^i$ angles almost planar (Table 2). Such value is to compare with the distortion in known $[MPz_4Cl_2]$ complexes; Mn: $4.6•10^{-3}$ [56], Ni: $7.5•10^{-3}$ [59] and Cu: $2.9•10^{-2}$ [61].

This structure is stabilized by weak inter- and intramolecular hydrogen bonds (Table 3). Opposing Pz ligands are coplanar with one another but inverted through $Co^{2+}$, with no significant canting of the ligand with respect to the Cl–Co(II)–Cl axis. The crystal packing involves intermolecular $\pi$–$\pi$ stacking between Pz ligands of neighboring complexes along the crystallographic *c*-axis, forming repeating sets of two mirrored columns of complexes along the crystallographic *a*-axis (Fig. 1c). The channels are slightly canting to accommodate the ligand interactions, the dihedral angle between the facing Pz is of 75.2° Hydrogen bonding between $Cl^-$ and the Pz N–H proton occurs with a Cl…H distances as depicted on Table 3. Similar such H-bonds ensure the cohesion between neighboring channels as shown in Fig. 1c.

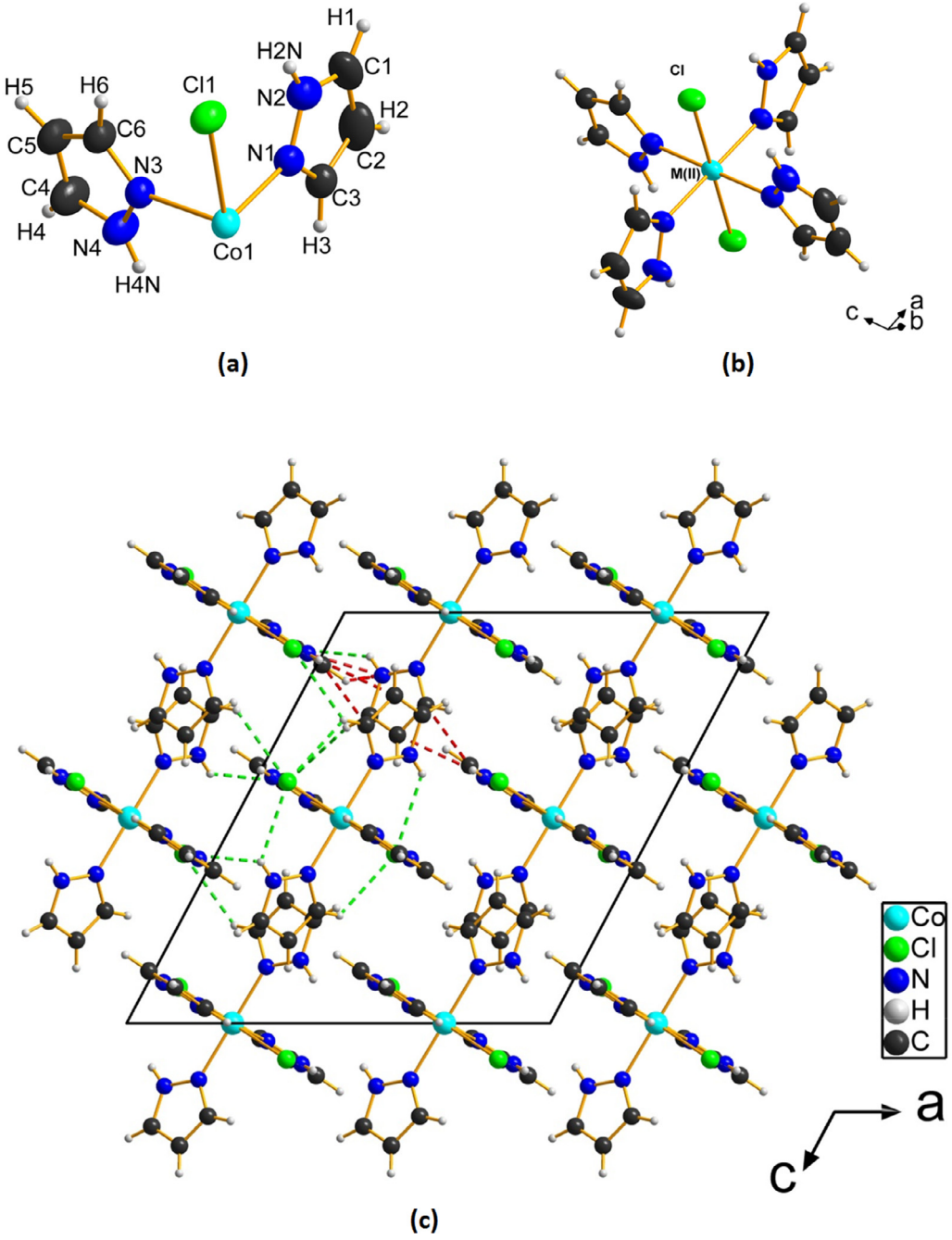


**Fig. 1.** (a) Asymmetric unit of (**1**), ellipsoids drawn at 50%; (b) discrete [$MPz_4Cl_2$] unit in the crystal structure of (**1**)-M(II), *M* = Mn, Co, Ni and Cu; and (c) a projection along [010] of the crystal structure of (**1**), dashed lines represent the H-bonds forming and linking the defined channels.

*3.1.2. Topological analysis*

The crystallographic packing can be more conveniently described using a typical topological approach in which the networks are simplified to central nodes and bridging rods. Based on pure mathematical concepts applied to crystal chemistry and by taking into consideration the connectivity of the individual building blocks, this procedure provides the immediate taxonomy of the structural frameworks, allowing consequently the comparison of the studied structures with the similar ones reported in the literature [76–80]. The topological studies were performed using the software package ToposPro [81].

Accordingly, the *standard representation* of the title compound performed by taking into account the cobalt cations, the pyrazole ligands and the counter-ions as the central nodes of the net, where the nodes are the gravity centers of each unit, gave a 0-periodic binodal 1,6-connected ⟨13:bold ⟩1,6M7–1⟨/13:bold⟩ underlying net, with stoichiometry $(1\text{-c})_6(6\text{-c})$ (Fig. 2a). The title compound share this topology with the other isostructural complexes mentioned above (**2**) [56,57], (**3**) [58,59] and (**4**) [60–68], assuming that they all were analyzed over the *standard representation* of coordination compounds and valence-bonded MOFs.

In order to simplify the structure further (Fig. 2b), it could be analyzed over another simplified description by adopting the same simplification means of the molecular structure linked through all the existing hydrogen bonds and *van der Waals* interactions built up from the counter-ions as acceptors (Fig. 3a). Thus, if the discrete molecules of the title complex are regarded as 14-connected nodes (Fig. 3b), the resulting three-dimensional framework can be

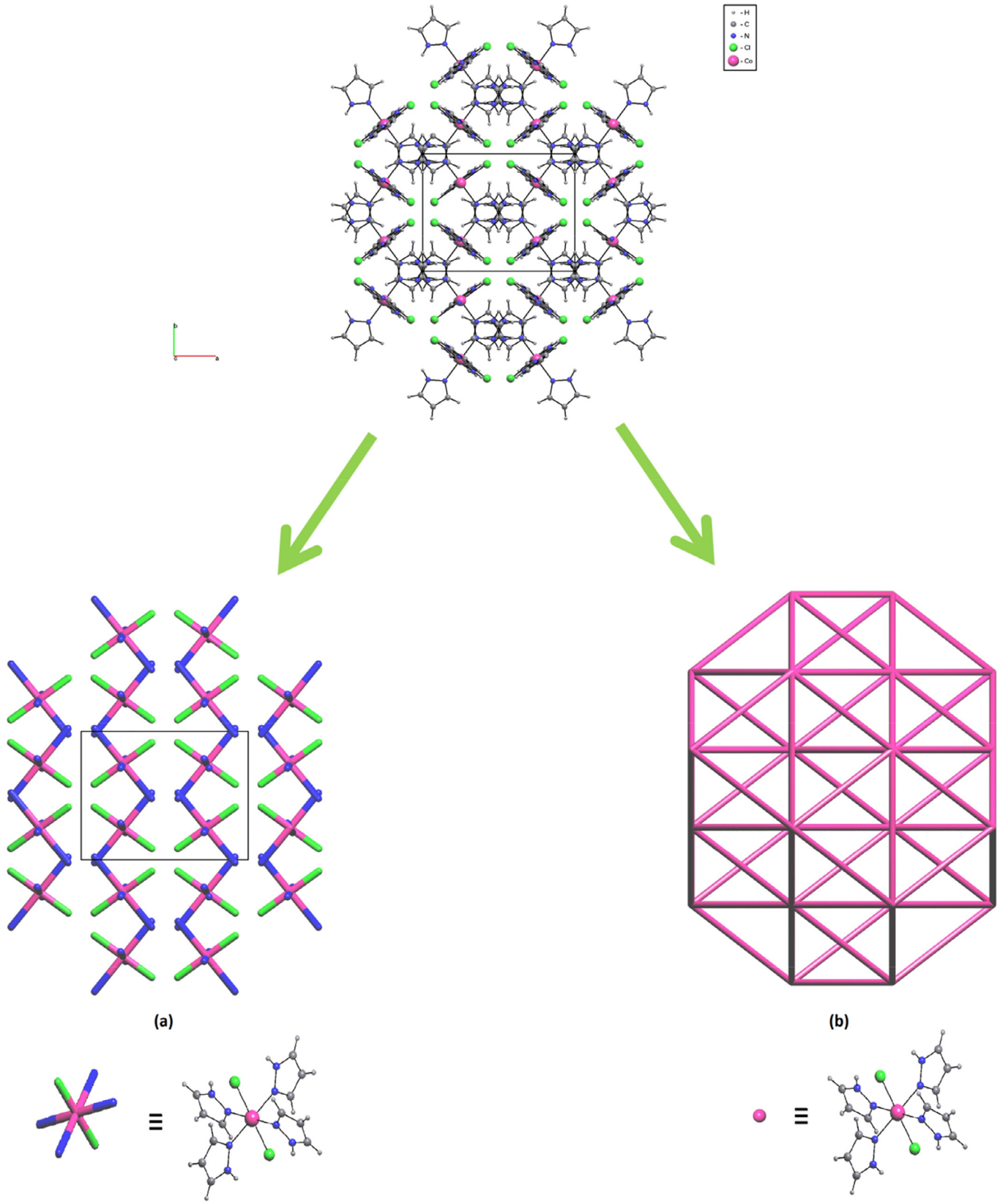


**Fig. 2.** Topological views through the *c*-axis of (a) the 0-periodic binodal simplified net; and (b) the three-dimensional **bcu-x** framework.

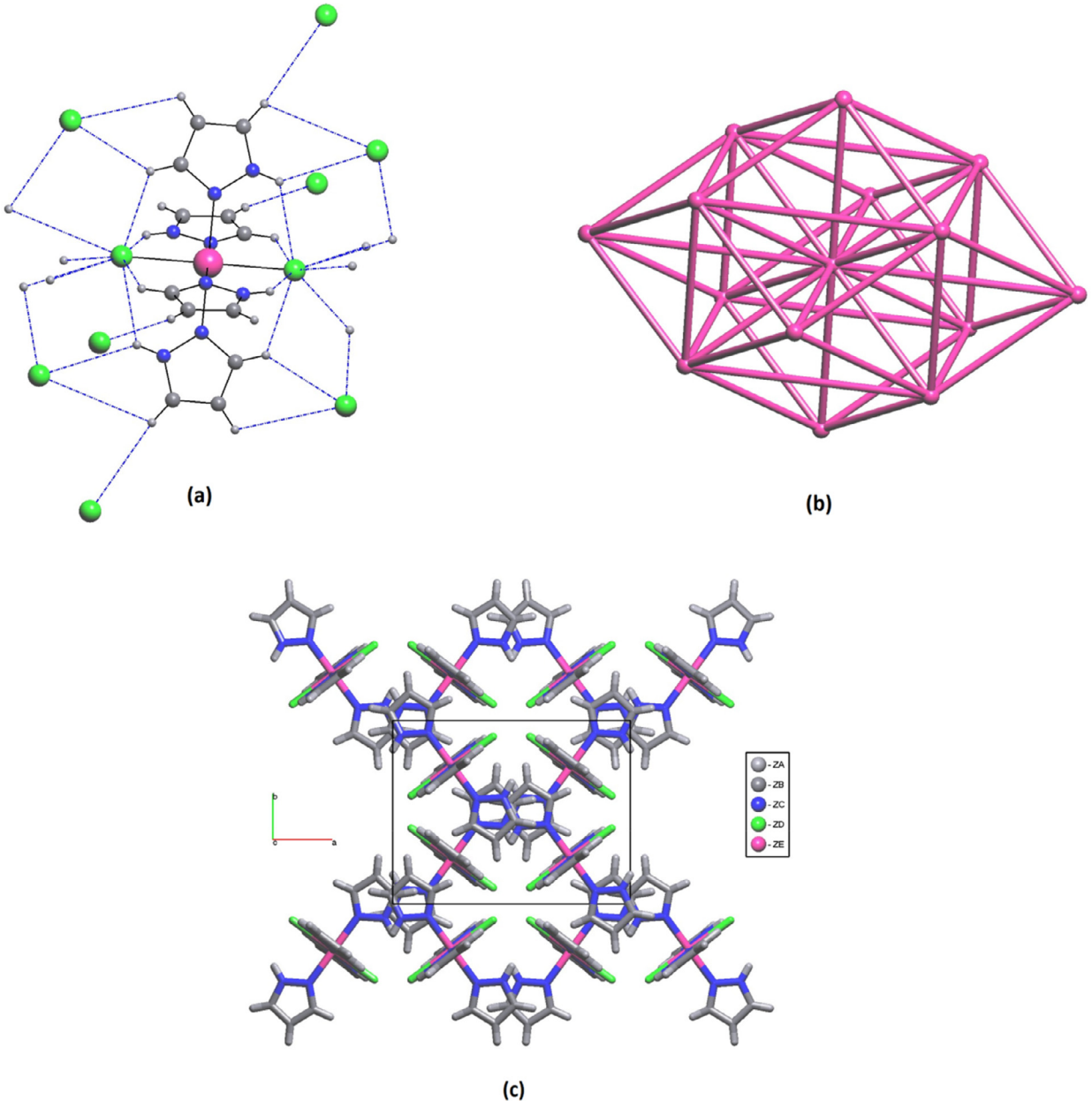


**Fig. 3.** (a) Hydrogen bonds and *van der Waals* interactions around the discrete complex molecules adopted in the simplification procedure; (b) a schematic representation of the resulting 14-connected nodes; and (c) the new 7-nodal topology resulting from the *standard representation* of covalent and ionic compounds.

ultimately reduced to a 14-connected uninodal body-centered cubic **bcu–x** net [82] (referenced as **sqc38** in the EPINET [83]), as shown in Fig. 2b, with the point symbol ($3^{36}.4^{48}.5^{7}$). Furthermore, by considering the centroids of each atomic entity composing the title complex, the structure could be simplified to a new topological 7-nodal $1^3$,$3^3$,6-connected underlying net, with stoichiometry (1-c)$_8$(1-c)$_8$(1-c)$_2$(3-c)$_8$(3-c)$_8$(3-c)$_4$(6-c), as a *standard representation* of covalent and ionic compounds, as depicted in Fig. 3c.

### 3.1.3. Hirshfeld surface analysis

Traditional hydrogen bonding, *van der Waals* forces, and non-classical $\pi\ldots\pi$ and C–H$\ldots\pi$ interactions play important roles in stabilizing the crystal packing of solid-state materials. In order to explore the nature of the intermolecular interactions found in the title compound, to quantify them and estimate their contribution toward its crystal structure stability, a detailed *Hirshfeld* surface analysis of (**1**) was performed. The *Hirshfeld* surfaces **HS**s, the fingerprint plots **FP**s, the interaction energies and the energy frameworks [84] were calculated using CrystalExplorer17 [85]. The complete and the decomposed 2D **FP**s for the title complex visualizing the overall distribution and the percentage contribution of each contact are shown in Fig. 4. The largest contribution over the total **HS** of 54.2% was observed for the H…H contacts, which are found to be located in the middle of the scattered points in the **FP** (Fig. 4b) with a shortest distance corresponding to $d_e = d_i \sim$ 1.18 Å and the close interaction C1—H1…H3—C3/C3—H3…H1—C1 highlighted on the *curvedness* representation (Fig. 5a).

The next two contacts with the second significant contributions to the total **HS** are H…C/H…C (Fig. 4c) and H…Cl/Cl…H (Fig. 4d) which cover respectively 21.8% and 11.0% of the overall surface. They consequently reveal the existence of the N—H…$\pi$/$\pi$…H—N (and C—H…$\pi$/$\pi$…H—C) and C—H…Cl/Cl…H—C (and N—H…Cl/Cl…H—N) interactions which are visualized as deep-red spots between the corresponding donors and acceptors on the

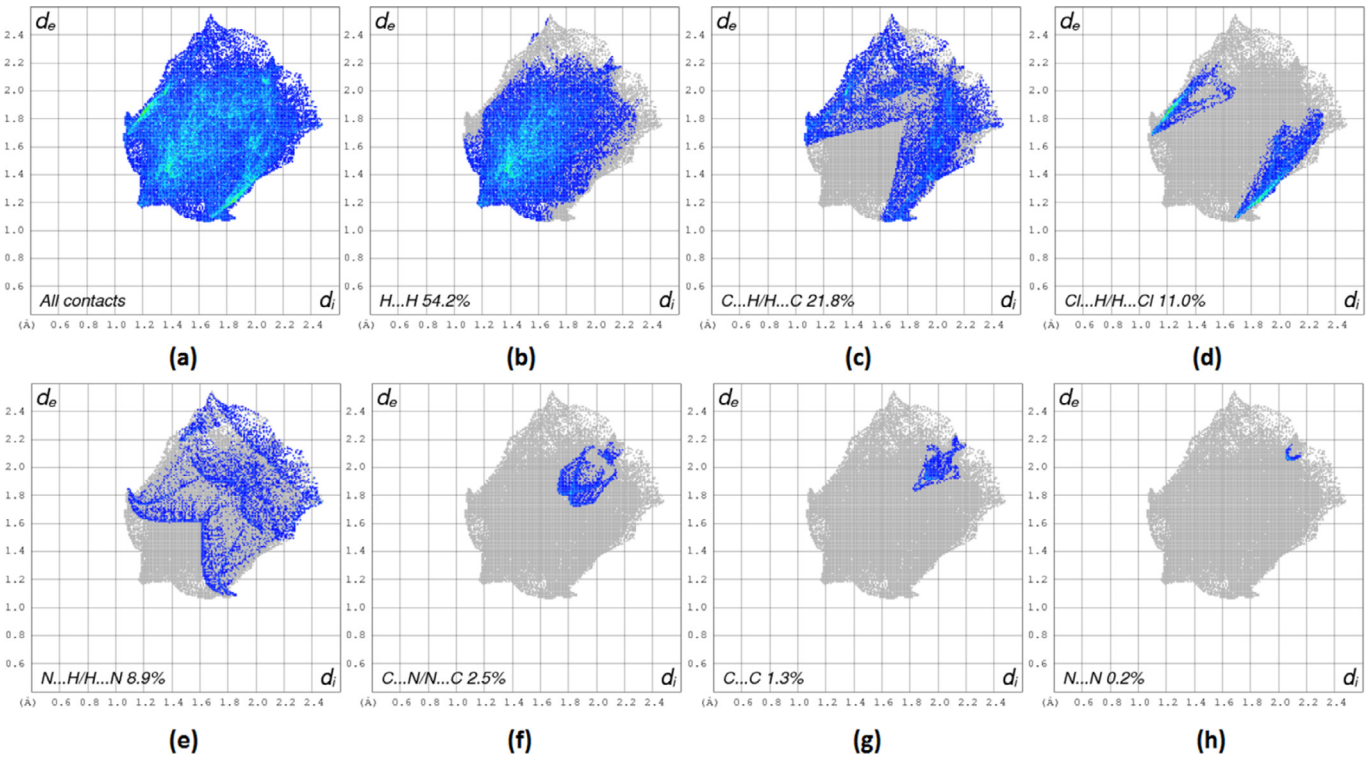


**Fig. 4.** Graphical representation of the (a) 2-dimensional fingerprint plot and the decomposed ones showing the relative contribution of the various (b) H…H, (c) C…H/H…C, (d) Cl…H/H…Cl, (e) N…H/H…N, (f) C…N/N…C, (g) C…C and (h) N…N contacts around the cocrystal of the title compound.

**HS** mapped over $d_{norm}$ (Fig. 5b). This is confirmed by the **HS** displayed as the $d_i$ and $d_e$ representations showing the reciprocal shortest interactions N4–H4…C2 (Fig. 5c) and C2…H4–N4 (Fig. 5d) appearing at $d_e + d_i \sim 2.70$ Å. Additionally, the **HS** mapped over $d_{norm}$ (Fig. 5b) exhibits another short interaction, being 2.70 Å long, involving N4 as a donor and C3 as an acceptor. As for the shortest hydrogen bond C3—H3…Cl1 described above in the crystal structure description section, it appears as two sharp long spikes in the corresponding **FP** (Fig. 4d) at about $d_e + d_i \sim 2.80$ Å and is depicted in Fig. 5b by generating a $d_{norm}$ surface.

Fig. 4e shows the distribution of the N…H/H…N contacts indicated as two wings, in the upper left and lower right of the **FP**, and their proportion of about 8.9% resulting from the C4–H4…N2/N2…H4–C4 intermolecular interactions which correspond to a short length of around 2.8 Å. Furthermore, the presence of the C…N/N…C and N…N contacts reflects the presence of the *van der Waals* $\pi$…*lp*/*lp*…$\pi$ and *lp*…*lp* interactions, which comprise respectively 2.5% (Fig. 4f) and 0.2% (Fig. 4h) of the total **HS** area with respectively $d_e + d_i \sim 3.55$ Å and $d_e = d_i \sim 2.5$ Å. The C…C contacts count only for 1.3% of the overall **HS** (Fig. 4g). Accordingly, no significant $\pi$…$\pi$ stacking are observed and the closest ring centroid-to-ring centroid distance is about 3.68 Å.

### 3.1.4. Interactions energy (IE) and energy frameworks (EF) analysis

In order to shed a light on the interaction topology in the crystal packing of (**1**), energy framework analysis was performed, in which the values of interaction energies **IE** are used to construct the three-dimensional topology of interactions that are termed as energy frameworks **EF**s [84,86]. Therefore, the **IE**s between pairs of molecules were obtained by applying the CE-B3LYP/6–31G(*d,p*) functional/basis set combination. The **IE** is broken down as:

$$E_{tot} = E_{ele} + E_{pol} + E_{dis} + E_{rep}$$

$$k_{ele}\, E'_{ele} + k_{pol}\, E'_{pol} + k_{dis}\, E'_{dis} + k_{rep}\, E'_{rep}$$

where the *k* values are scale factors with $E_{ele}$ stands for the *electrostatic component*, $E_{pol}$ the *polarization energy*, $E_{dis}$ the *dispersion energy* and $E_{rep}$ the *exchange-repulsion energy* [86,87]. Table 4 shows the results of the **IE** calculations for (**1**) given by respective colors. The total energies of the possible intermolecular interactions are in the range [−0.5, −41.1] kJ•mol$^{-1}$, whereas, the *lattice energy* for the title complex is found to be −191.4 kJ•mol$^{-1}$. The magenta-colored molecule with symmetry operation (*x*+½, *y*+½, *z*) located at about 8.24 Å from the centroid of the selected molecule has shown the highest total interaction energy $E_{tot}$ of −41.1 kJ•mol$^{-1}$, while the blue-colored one, being at a distance of 12.25 Å from the same centroid and having the symmetry code (-*x*, *y*, -*z*+½), has displayed the lowest total interaction energy of −0.5 kJ•mol$^{-1}$.

A view along the *c*-axis of the symmetry molecules around the central one are graphically highlighted in Fig. 6a by respective colors and the **EF** diagrams are further represented. In an **EF**, the cylinder radius correlates with the strength of the intermolecular interaction. Consequently, the weaker interactions are running through the vertical columns along [010] and the ones emerging transversely. However, the much stronger interactions are observed between molecules making up bigger bundles developing diagonally and crosswise the previously mentioned ones. Here, two different types of interactions interconnecting the vertical tubes in a zigzag fashion with different energies are observed; the large cylindrical tubes of the *total energy, dispersion* and *electrostatic terms* ($E_{tot}$ = −41.1 kJ•mol$^{-1}$, $E_{dis}$ = −13.9 kJ•mol$^{-1}$ and $E_{ele}$ = −28.0 kJ•mol$^{-1}$) and the large diameter ones with ($E_{tot}$ = −37.7 kJ•mol$^{-1}$, $E_{dis}$ = −49.5 kJ•mol$^{-1}$ and $E_{ele}$ = −11.1 kJ•mol$^{-1}$). Thus, these big diagonal cylinders, made of the N–H…Cl hydrogen bonding, have greater *electrostatic components* ($E_{ele}$ = −28.0 kJ•mol$^{-1}$) which shows that these hydrogen bonds result in significantly favorable intermolecular attractive forces, surpassing the strength of the columnar H…H contacts ($E_{ele}$ = −8.2 kJ•mol$^{-1}$) and the intercolumnar *van der Waals* C—H…$\pi$, C—H…*lp* ($E_{ele}$ = −11.1 kJ•mol$^{-1}$) interactions. Furthermore, the *total interaction energy* and the *dis-*

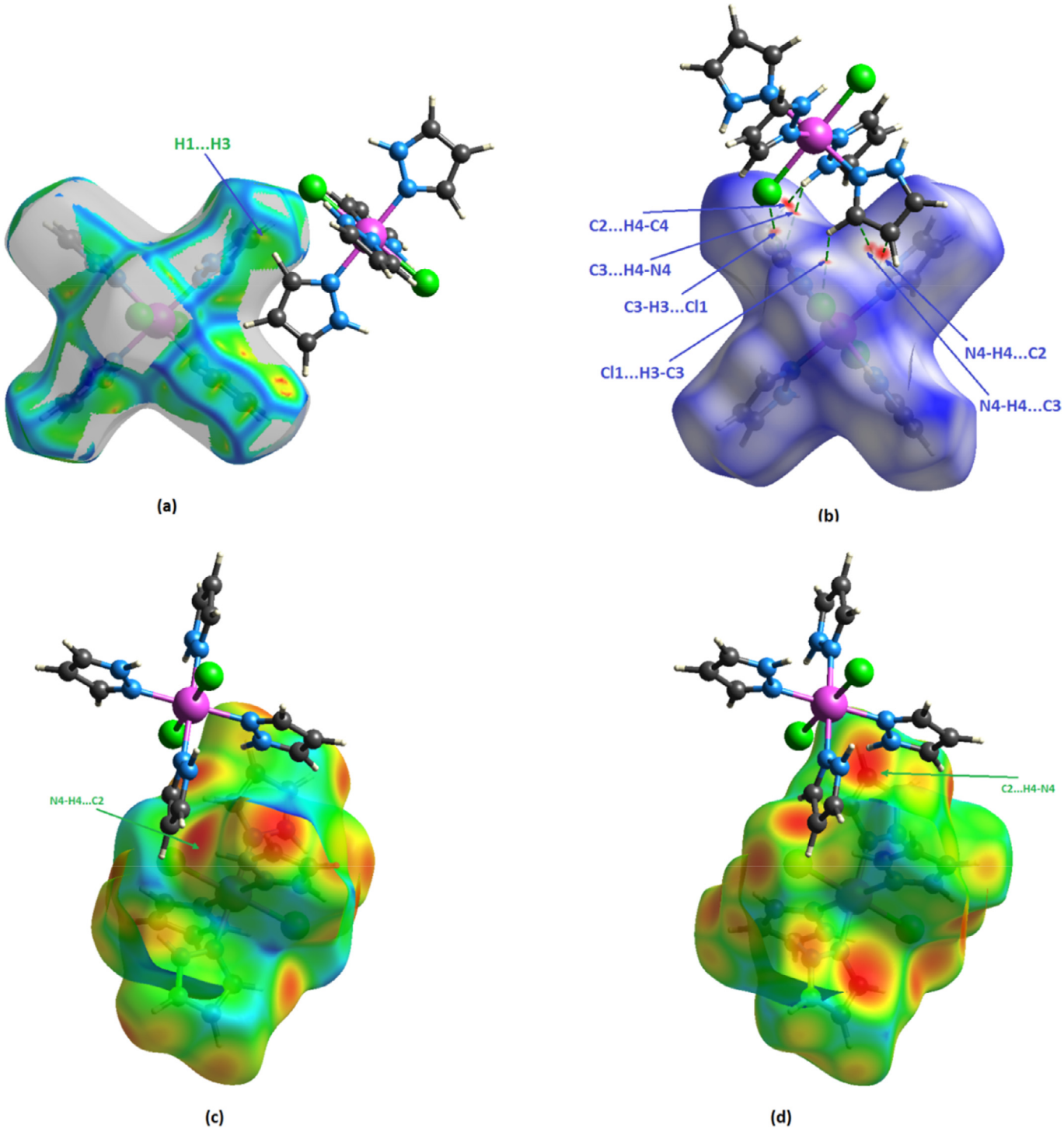


**Fig. 5.** (a) Shortest H...H contact drawn on the *curvedness* representation; (b) **HS** mapped with $d_{norm}$ showing the N—H...$\pi$/$\pi$...H—N and C—H...Cl/Cl...H—C interactions; (c) $d_i$; and (d) $d_e$ surfaces resulting from the shortest N4–H4...C2 and C2...H4–N4 interactions.

**Table 4**
Interaction energies in the framework of (1) (kJ•mol$^{-1}$). *N* refers to the number of molecules with an *R* molecular centroid-to-centroid distance (Å).

| *N* | Primary interaction | Symmetry code | *R* | $E'_{ele}$ | $E'_{pol}$ | $E'_{dis}$ | $E'_{rep}$ | $E'_{tot}$ |
|---|---|---|---|---|---|---|---|---|
| 2 | H...H | *x, y, z* | 9.29 | −12.2 | −3.5 | −15.6 | 11.7 | −21.9 |
| 4 | C–H...Cl, H...H | -*x*+½,*y*+½, -*z*+½ | 8.80 | −8.2 | −2.2 | −29.2 | 17.5 | −24.9 |
| 2 | N—H...$\pi$, C–H...Cl | -*x, y*, -*z*+½ | 7.39 | −16.9 | −8.9 | −46.6 | 39.9 | −40.4 |
| 2 | C—H...$\pi$, C—H...*lp* | *x*+½,*y*+½, *z* | 8.24 | −11.1 | −2.7 | −49.5 | 31.0 | −37.7 |
| 2 | $\pi$...$\pi$, C—H...$\pi$ | -*x, y*, -*z*+½ | 12.25 | 1.1 | −0.1 | −1.8 | 0.0 | −0.5 |
| 2 | N–H...Cl | *x*+½,*y*+½, *z* | 8.24 | −28.0 | −6.5 | −13.9 | 8.7 | −41.1 |

Scale factors used to calculate $E_{tot}$: $k_{ele}$ = 1.057, $k_{pol}$ = 0.740, $k_{dis}$ = 0.871 and $k_{rep}$ = 0.618 [87].

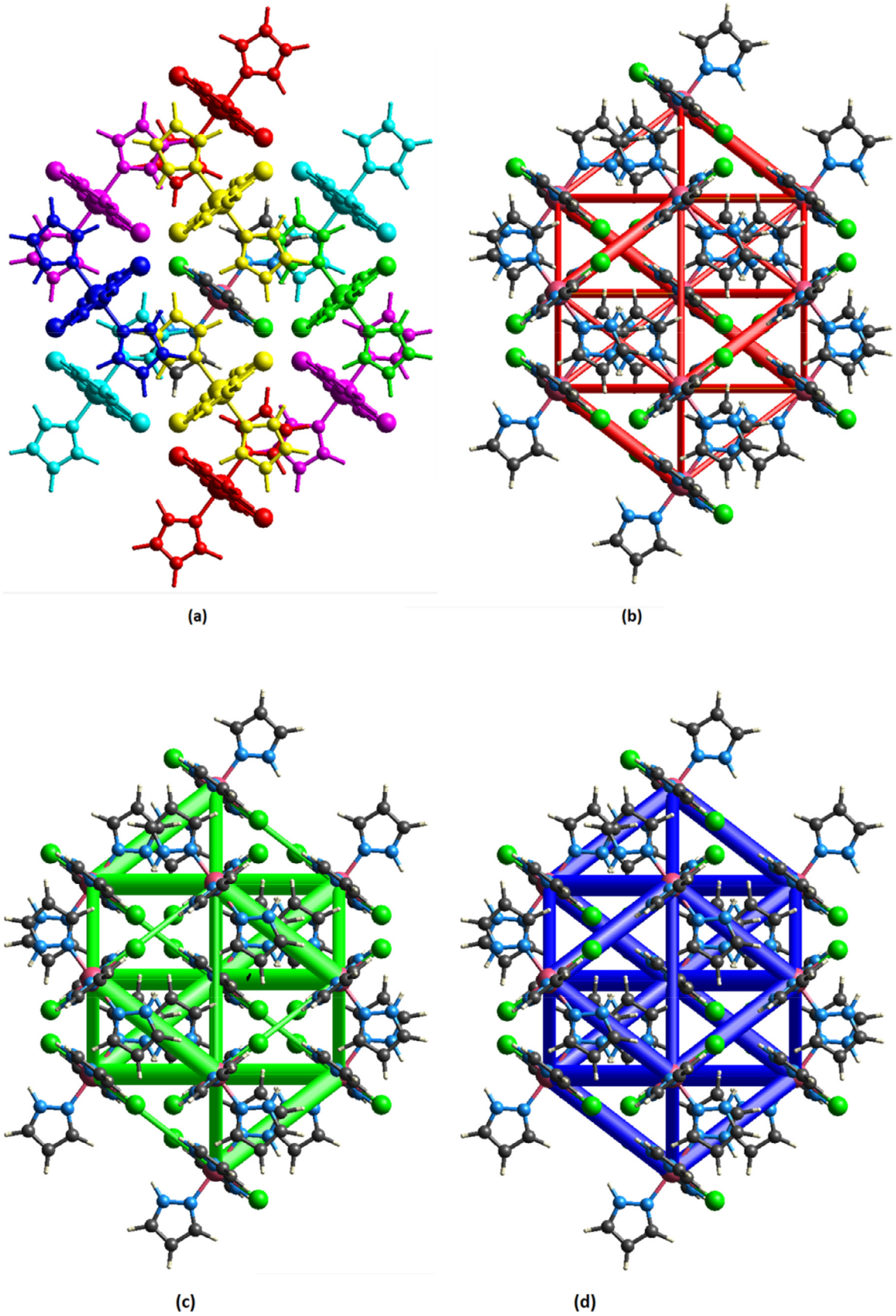


**Fig. 6.** (a) Color coding of neighboring molecules with respect to the central molecule; (b) **EF** diagrams viewed through the *c*-axis of the separate electrostatic; (c) dispersion components of (1); and (d) the corresponding total interaction energy. The energy factor scale is 80.

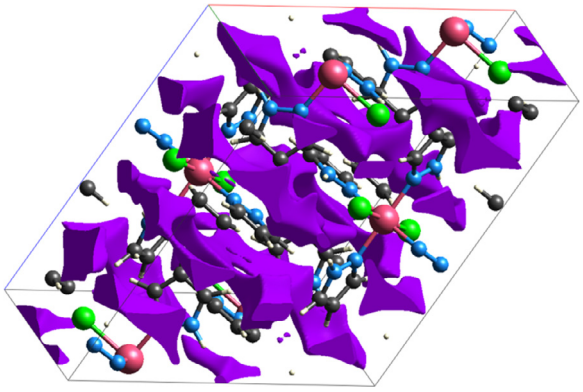

**Fig. 7.** A perspective view of the voids in (**1**) mapped at the 0.002 a.u. isosurface.

*persion term* for (**I**) show parallel horizontal cylindrical tubes with large diameters across the (*ac*) planes in which the intercolumnar N–H…$\pi$ and C–H…Cl interactions occur ($E_{tot}$ = −40.4 kJ•mol$^{-1}$ and $E_{dis}$ = −46.6 kJ•mol$^{-1}$).

From the **EF** analysis, it can be said that the *dispersion components* dominate the *electrostatic* ones of the *total interaction energies*, with one exception, namely the diagonal crosswise interaction found at 8.24 Å, which indicates the strength of the N–H…Cl hydrogen bond. These findings show that it can be consequently said that the magnitude of the *dispersion energies* closely mirrors the *total energies*; and thus the *electrostatic term* is mainly canceled by repulsion.

#### 3.1.5. Void mapping

The empty space in the crystal lattice of (**1**) was analyzed using *void mapping* which is related to the anisotropic properties of the molecular solid. The mapping of void space in the crystal lattice is presented by rolling a probe sphere of the variable radius over the **HS** [88]. Hence, Fig. 7 highlights the voids within the title complex mapped by constructing isosurfaces of the *procrystal* electron density of 0.002 a.u. The *surface area* is found to be 546.66 Å$^2$ and the calculated *voids volume* is 141.35 Å$^3$, while the volume of the unit cell is 1672.2 Å$^3$ leading consequently that the percentage of the voids in the unit cell of (**1**) worth 8.45% which confirms that the cavities are not large.

### 3.2. Computational results

#### 3.2.1. Geometric structure at ground state

The optimized structures of the title complex are calculated at the mentioned calculation levels and represented in Fig. 8a. The experimental and calculated geometric parameters given in Table 2 compare well.

In order to determine the best calculation method which will be adopted for the remaining calculations, the distribution graphs were plotted by using both the experimental and calculated results. Thus, the regression coefficients ($R^2$) are calculated as 0.7268, 0.9985, 0.9348 and 0.998 for bond lengths in HF method, bond angles in HF method, bond lengths in B3LYP method and bond angles in B3LYP method, respectively. These graphs are represented in Fig. 8b, and show that the best method reproducing the experimental data is B3LYP. Especially, for the bond lengths in the B3LYP method which are calculated quite well. However, the bond angles are similar in each calculation level. Therefore, B3LYP method is taken into consideration for the other calculation stages.

#### 3.2.2. MEP map and contour diagram of SOMO and LUMO

Molecular electrostatic potential (MEP) map are important to investigate the active regions, hence, the MEP map of (**1**) was calculated and represented in Fig. 9a. In this map, electronically rich regions are mainly displayed in red or yellow while electronically poor ones are shown in blue. Blue regions are dominant around the hydrogen atoms in the title complex, while red regions, appropriate for nucleophilic attacks, are mainly situated around the chlorine atoms.

Energy diagram of molecular orbitals, contour diagram of $\alpha$-SOMO and $\alpha$-LUMO are represented in Fig. 9b which shows that the energy gap is calculated as to be 4.493 eV. The $\alpha$-molecular orbitals play an important role in the determination of the studied complex reactivity. Therefore, there is an electron in the SOMO delocalized on the cobalt and the chlorine atoms. Additionally, there are big balloons around the chlorine atoms than that of the cobalt center, implying that the chlorine atoms will be more reactive if the complex provides electron. As for the LUMO, the title complex may accept electrons which will be delocalized on the cobalt and the nitrogen atoms.

#### 3.2.3. Estimation of the NLO properties

Non-linear optical properties (NLO) are significant in telecommunications and optical interactions. NLO properties increase with the delocalization of the $\pi$ electrons and the molecular planarity. We investigated the NLO properties of the studied complex through some quantum chemical descriptors (QCDs), which are the energy of the highest occupied molecular orbital ($E_{HOMO}$), the energy of the lowest unoccupied molecular orbital ($E_{LUMO}$), the ionization energy (I), the electron affinity (A), the energy gap ($E_{GAP}$), the absolute hardness ($\eta$), the absolute softness ($\sigma$), the optical softness ($\sigma_O$), the absolute electronegativity ($\chi$), the chemical potential (CP), the additional electronic charges ($\Delta N_{Max}$) and the polarizability ($\alpha$) calculated by applying Eqs. (1) – (9) and given in Table 5.

QCDs are useful in the determination of the NLO properties in the gas phase. These parameters only give suggestion about the studied complex. Thus, the first descriptor is the energy of HOMO. If the energy level of HOMO is high, the electrons in HOMO move more easily and can pass to upper levels. Since NLO activity of molecules increases with the increasing of electron mobility, the NLO properties of molecules will increase with the increasing of the energy level of HOMO. The second parameter is the energy of LUMO. The lower energy level of LUMO means that the electrons can be easily indwelled in LUMO. Therefore, the NLO activity increases with the decreasing of the LUMO energy level. The other parameter is the energy gap between HOMO and LUMO. The decreasing of this parameter means the increasing of the electron mobility and this supports the increase of the NLO properties. The absolute chemical hardness and softness are other important parameters. Therefore, the increasing of the chemical softness or the decreasing of the chemical hardness means the increasing of the molecules polarizability, which is directly correlated with the NLO activity. Additionally, the increasing of the optical softness means the increasing of the NLO properties. Furthermore, the electron delocalization increases with the decreasing of the absolute electronegativity. Moreover, there is a direct correlation between the NLO activity and the chemical potential. As for the electronic charge, it is related to the polarizability of molecule; the higher the value is, the more active the compound is in NLO applications. The last parameter is the polarizability; the NLO properties increase with the increasing of the mentioned descriptors. Thus, the general ranking is given as follow: (**1**) > Urea. The opposite ranking is obtained in terms of electronegativity and chemical potential. According to the above ranking, the NLO properties of (**1**) are better than that of urea and the title complex could be considered as a good candidate for NLO applications.

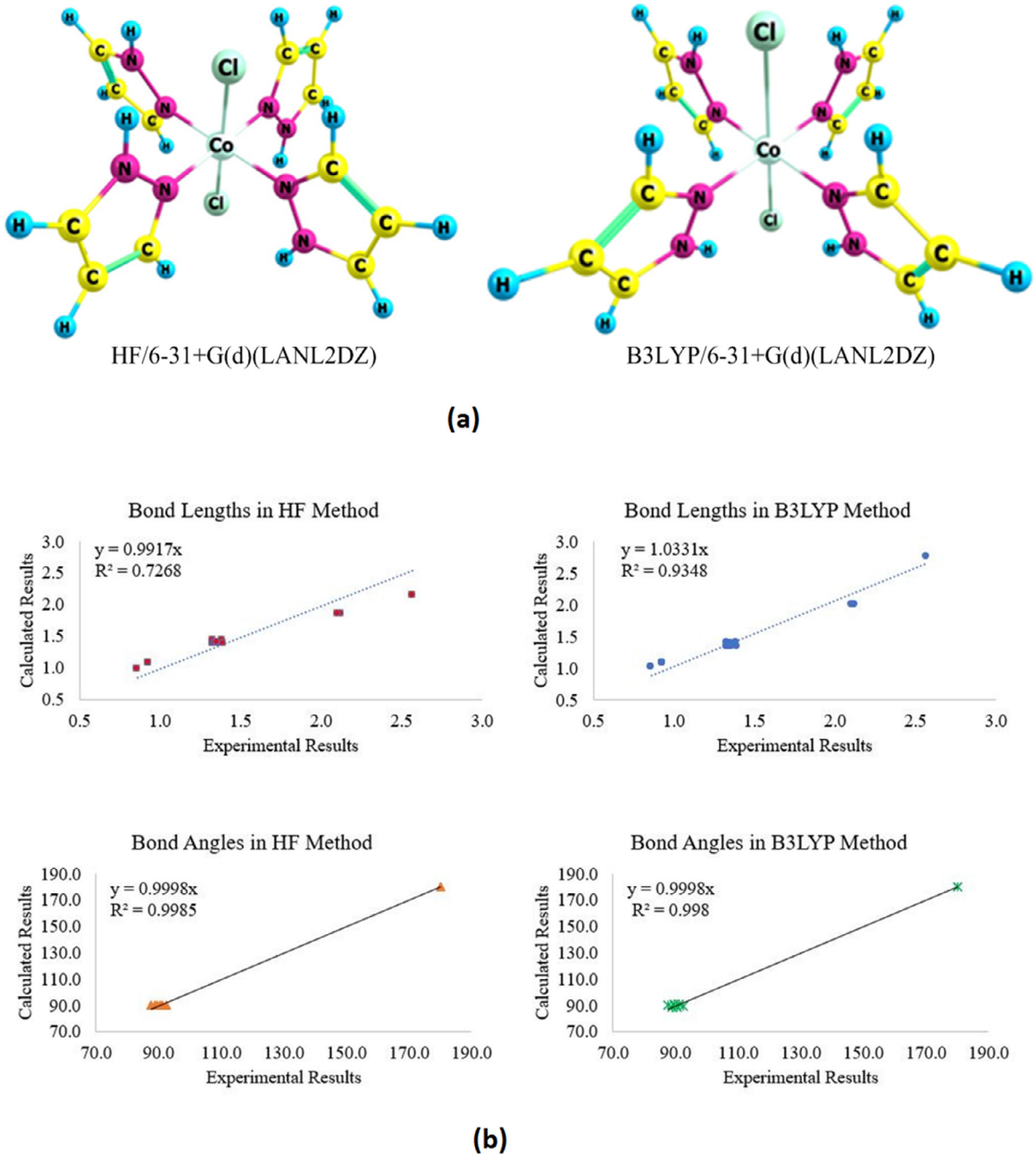


**Fig. 8.** (a) Optimized structures of the title complex at mentioned calculation levels in vacuum; and (b) distribution graphs of experimental and calculated results.

**Table 6**
Obtained data (in kcal•mol$^{-1}$) of the molecular docking calculations.

| Protein | Docking Score | *van der Waals* Energy | Coulomb Energy | Total Interaction Energy |
|---|---|---|---|---|
| 1JIL | −2.690 | −27.127 | 0.000 | −27.127 |
| 1B8A | −3.072 | −31.415 | 0.000 | −31.415 |

### 3.3. Optical and photoluminescence properties

The optical properties evaluation of the title complex is carried out by measuring its absorbance UV spectrum which exhibits an absorption band maximum at 313 nm resulting from the $\pi \rightarrow \pi^*$ electron transitions characteristic of aromatic compounds. Whereas, the same transition was observed between 200 and 240 nm in the free ligand UV–Vis spectrum, which was experimentally investigated in the literature [89,90]. This bathochromic effect detected in the pyrazole complex demonstrates that under the influence of a 3*d* metal the electronic system of the ligand is stabilized and the aromaticity increased [91,92]. The same absorption band could be described as $d \rightarrow \pi^*$ metal–ligand charge transfer transitions [93]. The absorption spectrum of the studied complex, given in Fig. 10a, shows another absorption band centered at 426 nm, corresponding to the n $\rightarrow \pi^*$ ligand–ligand electronic transitions [94]. Additionally, (**1**) absorbs at 521 nm (with a shoulder at approximately 537 nm), an absorption band attributed

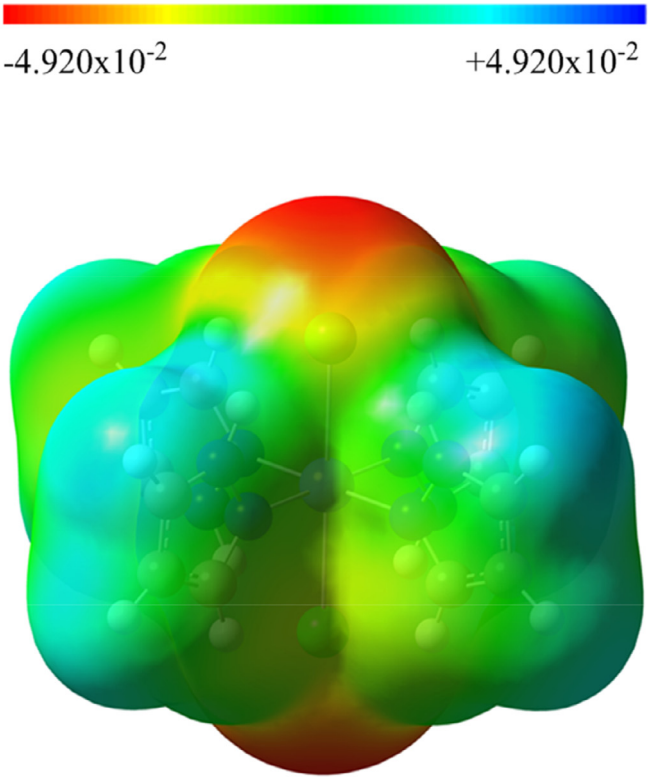


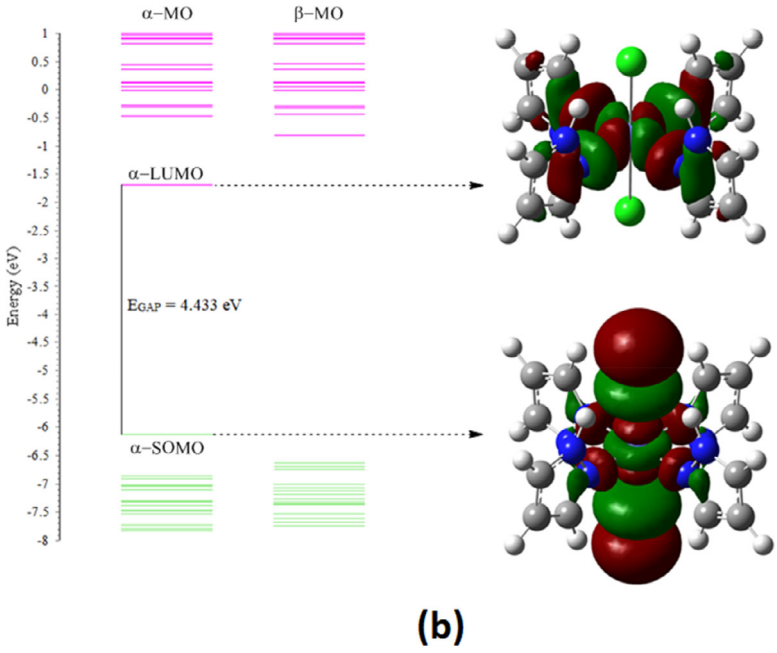


**Fig. 9.** (a) The MEP map of (**1**) at the same level of theory in gas phase; and (b) energy diagram of molecular orbital, contour diagram of $\alpha$-SOMO and $\alpha$-LUMO.

to the $d \rightarrow d$ transition indicative of a high spin octahedral Co(II) environment [95,96]. Furthermore, an absorption band pattern was observed at around 628 nm, which is probably due to the ligand-field transition [97].

The emission spectrum of the title complex measured at room temperature is shown in Fig. 10b It can be seen that the spectrum displays five photoluminescence bands and is hence dominated by the highest luminescence intensity centered at 652 nm which confirms the red light emission of the material originating tentatively from the ligand-field transition. Furthermore, the compound exhibits yellow-green photoluminescence bands concentrated at 533 and 551 nm, which were assigned to $d \rightarrow d$ transitions. A blue photoluminescence highlighted by the wavelength located at around 450 nm was additionally observed and as-

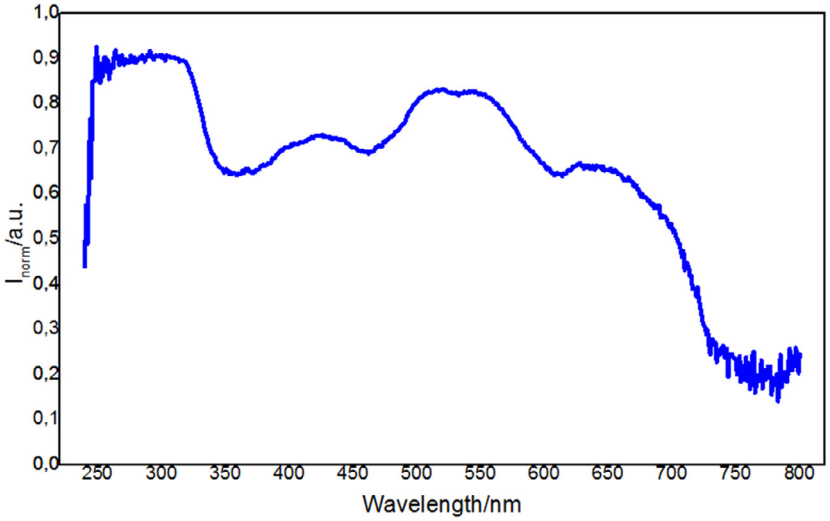


(a)

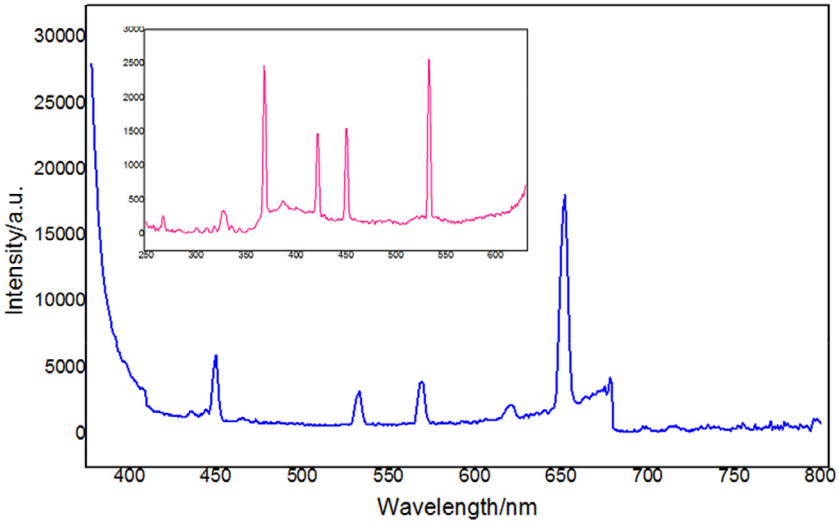


(b)

**Fig. 10.** (a) Optical absorption spectrum measured at room temperature; and (b) fluorescence emission spectrum of the title compound.

**Table 5**
Calculated quantum chemical descriptors at the same level of theory in gas phase.

| Compound | $E_{HOMO}$[a] | $E_{LUMO}$[a] | I[a] | A[a] | $E_{GAP}$[a] | $\eta$[a] |
|---|---|---|---|---|---|---|
| (I) | −6.118 | −1.685 | 6.118 | 1.685 | 4.433 | 2.216 |
| Urea | −7.314 | −0.372 | 7.314 | 0.372 | 6.942 | 3.471 |
| Compound | $\sigma$[b] | $\sigma_0$[b] | $\chi$[a] | CP[a] | $\Delta N_{Max}$ | $\alpha$[c] |
| (I) | 0.451 | 0.226 | 3.902 | −3.902 | 1.760 | 245.662 |
| Urea | 0.288 | 0.144 | 3.843 | −3.843 | 1.107 | 32.505 |

[a] in eV.
[b] in $eV^{-1}$.
[c] in a.u.

signed to the intra-ligand electronic transitions. Whereas, the band recorded at 368 nm, it arises from metal-to-ligand charge transfers. Accordingly, it can be concluded that the result of the strong red emission at 652 nm suggests that the studied compound can be used as a new red light emitting material.

### 3.4. Molecular docking

Molecular docking calculations are the most popular way to show the biological properties of compounds. In this manuscript, the activity of the title complex against **1JIL** and **1B8A** proteins was investigated. The receptor-ligand complex structures are shown in Fig. 11. Additionally, the docking score, the *van der Waals* energy, the coulomb energy and the total interaction energies are given in Table 6.

According to Table 6, there are no charge interactions in the results due to the fact that the coulomb energy is found to be zero. As for the *van der Waals* interactions, the calculated interaction energy is well for the ligand-receptor interaction. The main interaction types are determined as the polar interaction, the $\pi$ stacking interactions and solvent exposure in the calculations. Furthermore, the docking score implies the key-lock compatibility in the interactions. The calculated results of this parameter indicate that there

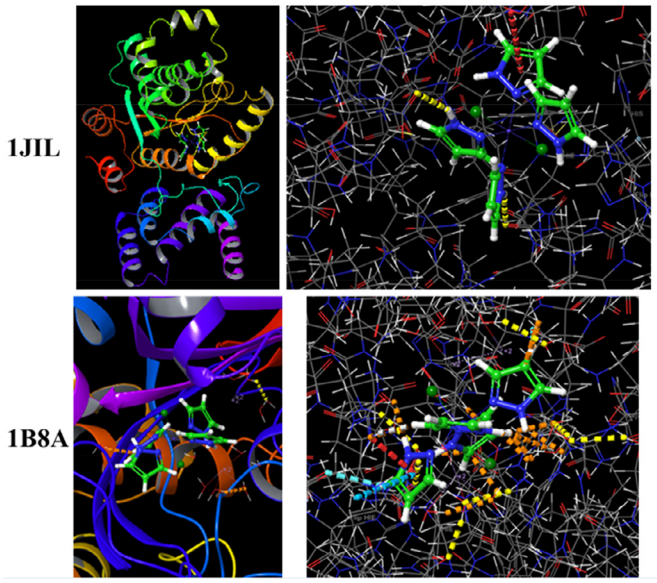


**Fig. 11.** Receptor-ligand structure in the studied Co(II) complex.

is a good compatibility between the receptor and the ligand. Consequently, the studied complex is appropriate in the inhibition of *Pyrococcus kodakaraensis* aspartyl-tRNA synthetase.

## 4. Conclusions

Block-like single crystals of a novel pyrazole-based Co(II) complex $[CoPz_4Cl_2]$ (**1**) were obtained and characterized. The X-ray crystal structure of the prepared material showed the presence of discrete $[MPz_4Cl_2]$ units linked together through weak inter- and intramolecular N—H…Cl and C—H…Cl hydrogen bonds forming a 14-connected uninodal **bcu-x** topology. By estimating the types and strengths of the non-covalent interactions found in this framework via the *Hirshfeld* surface analysis, non-classical H…H, N–H…C, C–H…N interactions and N—H…$\pi$, $\pi$…*lp*/*lp*…$\pi$, *lp*…*lp van der Waals* forces were observed in addition to the mentioned N—H…Cl and C—H…Cl hydrogen-bonding networks. Furthermore, the analysis of the optical properties of the title complex investigated at room temperature using optical absorption UV-visible and photoluminescence spectroscopy pointed out its interesting photoluminescence behavior with different emission intensities, particularly a bright red relaxation. The computational investigation of the title complex was performed by using HF and B3LYP methods with 6–31+G(d)(LANL2DZ) mix basis sets in gas phase. The structural analyses were performed in detail and the structural results in B3LYP/6–31+G(d)(LANL2DZ) was found to be better than that of HF method. The MEP maps, MOED, contour diagram of some molecular orbitals of (**1**) were examined. The NLO properties were investigated and the obtained results suggest that the studied complex could be a candidate for NLO applications. The molecular docking calculations were performed and show that the studied complex display an inhibition activity against *Pyrococcus kodakaraensis* aspartyl-tRNA synthetase.

## Credit author statement

**Amani DIREM:** Conceptualization, Writing - Original Draft, Writing - Review & Editing, Resources, Visualization, Validation. **Brahim EL BALI:** Writing - Original Draft, Visualization. **Koray SAYIN:** Resources, Writing - Original Draft. **Mohammed S. M. Abdelbaky:** Resources, Validation. **Santiago García-Granda:** Resources, Validation.

## Declaration of Competing Interest

None.

## CRediT authorship contribution statement

**Amani Direm:** Conceptualization, Writing - original draft, Writing - review & editing, Resources, Visualization, Validation. **Brahim El Bali:** Writing - original draft, Visualization. **Koray Sayin:** Resources, Writing - original draft. **Mohammed S.M. Abdelbaky:** Resources, Validation. **Santiago García-Granda:** Resources, Validation.

## Acknowledgments

Funding was provided by the General Direction of research and development technologies/Ministry of Higher Education and Research Sciences DGRSDT/MESRS, Algeria. The financial support from Abbes Laghrour University of Khenchela (Algeria), TUBITAK ULAKBIM, High Performance and Grid Computing Center (TR-Grid e-Infrastructure), Spanish MINECO (MAT2016–78155-C2–1-R), Gobierno del Principado de Asturias (GRUPIN-IDI/2018/000170) are acknowledged. This work is supported by the Scientific Research Project Fund of Sivas Cumhuriyet University under the project number RGD-020.

## References

[1] M.K. Kathiravan, A.B. Salake, A.S. Chothe, P.B. Dudhe, R.P. Watode, M.S. Mukta, S. Gadhwe, Bioorg. Med. Chem. 20 (2012) 5678.
[2] Y. Bansal, O. Silakari, Bioorg. Med. Chem. 20 (2012) 6208.
[3] H. Goker, C. Kus, D.W. Boykin, S. Yildiz, N. Altanlar, Bioorg. Med. Chem. 10 (2002) 2589.
[4] M. Boiani, M. Gonzalez. Mini, Rev. Med. Chem. 5 (2005) 409.
[5] O.O. Guven, T. Erdogan, H. Goker, S. Yildiz, Bioorg. Med. Chem. Lett. 17 (2007) 2233.
[6] B. Kupcewicz, M. Ciolkowski, B.T. Karwowski, M. Rozalski, U. Krajewska, I.P. Lorenz, P. Mayer, E. Budzisz, J. Mol. Struct. 1052 (2013) 32.
[7] S. Trofimenko, Prog. Inorg. Chem. 34 (1986) 115.
[8] S. Trofimenko, Chem. Rev. 93 (1993) 943.
[9] G.L. Monica, G.A. Ardizzoia, Prog. Inorg. Chem. 46 (1997) 151.
[10] S. Trofimenko, Chem. Rev. 72 (1972) 497.
[11] S. Trofimenko, in: Progressin Inorganic Chemistry, 34, Wiley-Interscience, New York, 1986, p. 115.
[12] A. Almasirad, M. Tajik, D. Bakhtiari, A. Shafiee, M. Abdollahi, M.J. Zamani, R. Khorasani, H. Esmaily, J. Pharmacy Pharmaceut. Sci. 8 (2005) 419.
[13] G. Mondal, H. Jana, M. Acharjya, A. Santra, P. Bera, A. Jana, A. Panja, P. Bera, Med. Chem. Res. 26 (2017) 3046.
[14] R. Kenchappa, Y.D. Bodke, A. Chandrashekar, S.K. M. ArunaSindhe, Peethambar. Arabian J. Chem. 10 (2017) S3895.
[15] O. Rosati, M. Curini, M.C. Marcotullio, A. Macchiarulo, M. Perfumi, L. Mattioli, F. Rismondo, G. Cravotto, Bioorg. Med. Chem. 15 (2007) 3463.
[16] A.A.M. Eissa, N.A.H. Farag, G.A.H. Soliman, Bioorg. Med. Chem. 17 (2009) 5059.
[17] P.A. Datar, S.R. Jadhav, Int. J. Med. Chem. 10 (2015) 2015Article ID 670181, 10 pages, 2015, doi:10.1155/2015/670181.
[18] S.K. Kashaw, V. Gupta, V. Kashaw, P. Mishra, J.P. Stables, N.K. Jain, Med. Chem. Res. 19 (2010) 250.
[19] A. Ansari, A. Ali, M. Asif, Shamsuzzaman, New J. Chem. 41 (2017) 16.
[20] M.A.-A. El-Sayed, N.I. Abdel-Aziz, A.A.-M. Abdel-Aziz, A.S. El-Azab, Y.A. Asiri, K.E.H. Eltahir, Bioorg. Med. Chem. 19 (2011) 3416.
[21] S. Mert, R. Kasimogullari, T. Ica, F. Colak, A. Altun, S. Ok, Eur. J. Med. Chem. 78 (2014) 86.
[22] K. Senga, T. Novinson, R.H. Springer, R.P. Rao, D.E. O'Brian, R.K. Robins, H.R. Wilson, J. Med. Chem. 18 (1975) 312.
[23] S.P. Singh, D. Kumar, Heterocycles 31 (1990) 855.
[24] F. Karcı, N. Şener, M. Yamaç, I. Şener, A. Demirçalı, Dyes Pigm. 80 (2009) 47.
[25] M. Sobiesiak, T. Muzioł, M. Rozalski, U. Krajewska, E. Budzisz, New J. Chem. 38 (2014) 5349.
[26] J. Liu, H. Zhang, C. Chen, H. Deng, T. Lu, L. Ji, Dalton Trans. 1 (2003) 114.
[27] R. Nagane, M. Chikira, M. Oumi, H. Shindo, W.E. Antholine, J. Inorg. Biochem. 78 (2000) 243.
[28] F. Arjmand, B. Mohani, S. Ahmad, Eur. J. Med. Chem. 40 (2005) 1103.
[29] J. Reedijk, Chem. Soc. Rev. 42 (2013) 1776.
[30] J. Perez, L. Riera, Eur. J. Inorg. Chem. (2009) 4913.
[31] J. Reedijk, Recl. Trav. Chim. Pays-Bas 89 (1970) 993.
[32] S.Q. Wang, F.F. Jian, Acta Crystallogr., Sect. E 64 (2008) M1532.
[33] G.M. Davies, H. Adams, M.D. Ward, Acta Crystallogr., Sect. C 61 (2005) M485.
[34] S. Bergner, G. Wolmershauser, H. Kelm, W.R. Thiel, Inorg. Chim. Acta 361 (2008) 2059.

[35] I.A. Guzei, L.C. Spencer, M.K. Ainooson, J. Darkwa, Acta Crystallogr., Sect. C 66 (2010) M336.
[36] J. Reedijk, B.A. Stork-Blaisse, G.C. Verschoor, Inorg. Chem. 10 (1971) 2594.
[37] M.C. Burla, R. Caliandro, B. Carrozzini, G.L. Cascarano, C. Cuocci, C. Giacovazzo, M. Mallamo, A. Mazzone, G. Polidori, J. Appl. Cryst. 48 (2015) 306–309.
[38] G.M. Sheldrick, Acta Cryst. C71 (2015) 3–8.
[39] L.J. Farrugia, J. Appl. Cryst. 45 (2012) 849–854.
[40] Oxford DiffractionCrysAlis CCD and CrysAlis RED. Versions (1.171.34.36), Oxford Diffraction Ltd., Abingdon, Oxford shire, England, 2010.
[41] K. Brandenburg, H. Putz, DIAMOND Version 3., 1251, Crystal Impact GbR, 2005 PostfachD-53002 Bonn, Germany.
[42] S.E. Kariper, K. Sayin, D. Karakaş, Theoretical study on the antitumor properties of Ru(II) complexes containing 2-pyridyl, 2-pyridine-4-carboxylic acid ligands, J. Mol. Struct. 1149 (2017) 473–486.
[43] K. Sayin, D. Karakaş, S.E. Kariper, T.A. Sayin, Computational study of some fluoroquinolones: structural, spectral and docking investigations, J. Mol. Struct. 1156 (2018) 172–181.
[44] G. Serdaroğlu, M. Elik, A Computational study predicting the chemical reactivity behavior of 1-substituted 9-ethyl-$\beta$CCM derivatives: DFT- based quantum chemical descriptors, Turk. Comput. Theoret. Chem. 2 (1) (2018) 1–11.
[45] R. Dennington, T. Keith, J. Millam, GaussView, Version 5, Semichem Inc., Shawnee Mission, KS, 2009.
[46] Gaussian 09, Revision A.02, M. J. Frisch, G. W. Trucks, H. B. Schlegel, G. E. Scuseria, M. A. Robb, J. R. Cheeseman, G. Scalmani, V. Barone, B. Mennucci, G. A. Petersson, H. Nakatsuji, M. Caricato, X. Li, H. P. Hratchian, A. F. Izmaylov, J. Bloino, G. Zheng, J. L. Sonnenberg, M. Hada, M. Ehara, K. Toyota, R. Fukuda, J. Hasegawa, M. Ishida, T. Nakajima, Y. Honda, O. Kitao, H. Nakai, T. Vreven, J. A. Montgomery, Jr., J. E. Peralta, F. Ogliaro, M. Bearpark, J. J. Heyd, E. Brothers, K. N. Kudin, V. N. Staroverov, R. Kobayashi, J. Normand, K. Raghavachari, A. Rendell, J. C. Burant, S. S. Iyengar, J. Tomasi, M. Cossi, N. Rega, J. M. Millam, M. Klene, J. E. Knox, J. B. Cross, V. Bakken, C. Adamo, J. Jaramillo, R. Gomperts, R. E. Stratmann, O. Yazyev, A. J. Austin, R. Cammi, C. Pomelli, J. W. Ochterski, R. L. Martin, K. Morokuma, V. G. Zakrzewski, G. A. Voth, P. Salvador, J. J. Dannenberg, S. Dapprich, A. D. Daniels, Ö. Farkas, J. B. Foresman, J. V. Ortiz, J. Cioslowski, and D. J. Fox, Gaussian, Inc., Wallingford CT, 2009.
[47] E. Harder, W. Damm, J. Maple, C. Wu, M. Reboul, J.Y. Xiang, J.W. Kaus, OPLS3: a force field providing broad coverage of drug-like small molecules and proteins, J. Chem. Theory Comput. 12 (1) (2016) 281–296.
[48] R.A. Friesner, R.B. Murphy, M.P. Repasky, L.L. Frye, J.R. Greenwood, T.A. Halgren, D.T. Mainz, Extra precision glide: docking and scoring incorporating a model of hydrophobic enclosure for protein– ligand complexes, J. Med. Chem. 49 (21) (2006) 6177–6196.
[49] R.A. Friesner, J.L. Banks, R.B. Murphy, T.A. Halgren, J.J. Klicic, D.T. Mainz, D.E. Shaw, Glide: a new approach for rapid, accurate docking and scoring. 1. Method and assessment of docking accuracy, J. Med. Chem. 47 (7) (2004) 1739–1749.
[50] Richard A. Friesner, et al., Glide: a new approach for rapid, accurate docking and scoring. 1. Method and assessment of docking accuracy, J. Med. Chem. 47 (7) (2004) 1739–1749.
[51] Schrödinger Release 2019-4: LigPrep, Schrödinger, LLC, New York, NY, 2019.
[52] Schrödinger Release 2019-4: Maestro, Schrödinger, LLC, New York, NY, 2019.
[53] X. Qiu, C.A. Janson, W.W. Smith, S.M. Green, P. McDevitt, K. Johanson, A. Fosberry, Crystal structure of Staphylococcus aureus tyrosyl-tRNA synthetase in complex with a class of potent and specific inhibitors, Protein Sci. 10 (10) (2001) 2008–2016.
[54] E. Schmitt, L. Moulinier, S. Fujiwara, T. Imanaka, J.C. Thierry, D. Moras, Crystal structure of aspartyl-tRNA synthetase from Pyrococcus kodakaraensis KOD: archaeon specificity and catalytic mechanism of adenylate formation, EMBO J. 17 (17) (1998) 5227–5237.
[55] J.G. Malecki (2015) dichloro-tetrakis(1H-pyrazole)-cobalt(ii), CSD Communication (Private Communication), CSD-Reference: PYRZCO01.
[56] P.O. Lumme, E. Lindell, I. Mutikainen, trans-Dichloro-tetrakis(pyrazole-N)-manganese(ii), Acta Crystallogr., Sect. C 44 (1988) 967 GEXJOI.
[57] W. Lerner, M. Bolte (2005) Dichloro-tetrakis(pyrazole)-manganese(ii), CSD Communication(Private Communication) GEXJOI01
[58] C.W. Reimann, A.D. Mighell, F.A. Mauer, Dichloro-tetrakis(pyrazole-N2)-nickel(ii), Acta Crystallogr. 23 (1967) 135.
[59] R.B. Helmholdt, W. Hinrichs, J. Reedijk, Dichloro-tetrakis(pyrazole-N2)-nickel(ii), Acta Crystallogr., Sect.C 43 (1987) 226 NIPYRA01 and NIPYRA02.
[60] A. Mighell, A. Santoro, E. Prince, C. Reimann, Dichloro-tetrakis(pyrazole-N)-copper(ii), Acta Crystallogr., Sect. B 31 (1975) 2479 CTPZCU.
[61] U Casellato, R Ettorre, R Graziani, Dichloro-tetrakis(pyrazol-2-yl)-copper(ii), Z. Kristallogr.-New Cryst.Struct. 215 (2000) 287 CTPZCU02.
[62] A.M. Mills, K. Flinzner, A.F. Stassen, J.G. Haasnoot, A.L. Spek (2002) Dichloro-tetrakis(pyrazole-N)-copper(ii), CSD Communication(Private Communication) CTPZCU03
[63] Y.-J. Sun, P. Cheng, S.-P. Yan, D.-Z. Liao, Z.-H. Jiang, P.-W. Shen, Dichloro-tetrakis(pyrazol-2-yl)-copper(ii), J.Mol.Struct. 597 (2001) 191 CTPZCU04.
[64] J. Han, B.-L. Zhang, X.-J. Zhang, Y.-H. Zhang, G.-H. Zhou, Dichlorotetrakis(1H-pyrazole-$\kappa$N2)copper(ii), Acta Crystallogr., Sect.E 62 (2006) m3354 CTPZCU05.
[65] E. Mutsenek, M. Bolte, Dichloro-tetrakis(1H-pyrazole)-copper(ii), CSD Communication, 2011 (Private Communication) CTPZCU06.
[66] A. Direm, M. Tursun, C. Parlak, N. Benali-Cherif, trans-Dichloro-tetrakis(1H-pyrazole-N2)-copper(ii), J. Mol. Struct. 1093 (2015) 208 CTPZCU07.
[67] I.D. Giles, J.C. DePriest, J.R. Deschamps, dichloro-tetrakis(1H-pyrazole)-copper(ii), J.Coord.Chem. 68 (2015) 3661 CTPZCU08.
[68] J.G. Malecki, dichloro-tetrakis(1H-pyrazole)-copper(ii), CSD Communication (Private Communication) CTPZCU09, 2015.
[69] C.W. Reimann, Chem. Commun. (1969) 145–146.
[70] G. Hanggi, H. Schmalle, E. Dubler, Inorg. Chem. 27 (1988) 3131.
[71] G. Hanggi, H. Schmalle, E. Dubler, Acta Crystallogr., Sect. C44 (1988) 1560.
[72] G. Hanggi, H. Schmalle, E. Dubler, Inorg. Chem. 32 (1993) 6095.
[73] C. Bergquist, G. Parkin, Inorg. Chem. 38 (1999) 422.
[74] K. Robinson, G.V. Gibbs, P.H. Ribbe, Science 172 (1971) 567.
[75] M.E. Fleet, Miner. Mag. 40 (1976) 531.
[76] L. Carlucci, G. Ciani, D.M Proserpio, Coord. Chem. Rev. 246 (2003) 247–289.
[77] L. Carlucci, G. Ciani, D.M. Proserpio, CrystEngComm 5 (2003) 269–279.
[78] I.A. Baburin, V.A. Blatov, L. Carlucci, G. Ciani, D.M. Proserpio, J. Solid State Chem. 178 (2005) 2452–2474.
[79] V.A. Blatov, L. Carlucci, G. Ciani, D.M. Proserpio, CrystEngComm 6 (2004) 377–395.
[80] O. Delgado-Friedrichs, M.D. Foster, M. O'Keeffe, D.M. Proserpio, M.M.J. Treacy, O.M. Yaghi, J. Solid State Chem. 178 (2005) 2533–2554.
[81] V.A. Blatov, A.P. Shevchenko, D.M. Proserpio, Applied topological analysis of crystal structures with the program package ToposPro, Cryst. Growth Des. 14 (2014) 3576–3586.
[82] M. O'Keeffe, M.A. Peskov, S.J. Ramsden, O.M. Yaghi, Acc. Chem. Res. 41 (2008) 1782–1789.
[83] R.J. Hill, D.L. Long, P. Hubberstey, M. Schroder, N.R. Champness, J. Solid State Chem. 178 (2005) 2414–2419.
[84] M.J. Turner, S.P. Thomas, M.W. Shi, D. Jayatilaka, M.A. Spackman, Chem. Commun. 51 (2015) 3735–3738.
[85] M.J. Turner, J.J. McKinnon, S.K. Wolff, D.J. Grimwood, P.R. Spackman, D. Jayatilaka, M.A. Spackman, CrystalExplorer17, University of Western Australia, 2017 http://crystalexplorer.scb.uwa.edu.au.
[86] M.J. Turner, S. Grabowsky, D. Jayatilaka, M.A. Spackman, J. Phys. Chem. Lett. 5 (2014) 4249–4255.
[87] C.F. Mackenzie, P.R. Spackman, D. Jayatilaka, M.A. Spackman, IUCrJ 4 (2017) 575–587.
[88] M.J. Turner, J.J. Mckinnon, D. Jayatilaka, M.A. Spackman, Visualisation and characterization of voids in crystalline materials, CrystEngComm 13 (2011) 1804–1813.
[89] B. Samir, C. Kalalian, E. Roth, R. Salghi, A. Chakir, RSC Adv. 9 (2019) 27361–27368.
[90] I.C. Walker, M.H. Palmer, M.J. Hubin-Franskin, J. Delwiche, Chem. Phys. Lett. 367 (2003) 517–522.
[91] W. Lewandowski, M. Kalinowska, H. Lewandowska, The influence of metals on the electronic system of biologically important ligands. Spectroscopic study of benzoates, salicylates, nicotinates and isoorotates, Review. J Inorg Biochem. 99 (2005) 1407–1423.
[92] W. Lewandowski, L. Fuks, M. Kalinowska, P. Koczoń, The influence of selected metals on the electronic system of biologically important ligands, Spectrochim Acta A 59 (14) (2003) 3411–3420.
[93] V.G. Vlasenko, D.A. Garnovskii, G.G. Aleksandrov, N.I. Makarova, S.I. Levchenkov, A.L. Trigub, Y.V. Zubavichus, A.I. Uraev, Y.V. Koshchienko, A.S. Burlov, Mixed ligand metal-complexes of tridentate N, N, S pyrazole containing Schiff base and 2-amino-1-ethylbenzimidazole: synthesis, structure, spectroscopic studies and quantum-chemical calculations, Polyhedron 133 (2017) 245–256.
[94] H.Y. Khan, M.O. Ansari, G.G.H.A. Shadab, S. Tabassum, F. Arjman, Evaluation of cytotoxic activity and genotoxicity of structurally well characterized potent cobalt(II) phen–based antitumor drug entities: an in vitro and in vivo approach, Bioorg. Chem. 88 (2019) 102963.
[95] F.E. Jacobsen, R.M. Breece, W.K. Myers, D.L. Tierney, S.M. Cohen, Model complexes of cobalt-substituted matrix metalloproteinases: tools for inhibitor design, Inorg. Chem. 45 (2006) 7306–7315.
[96] B. Boni Dias, F. Gomes da Silva Dantas, F. Galvão, W.J. Cupozak-Pinheiro, H. Wender, L. Pizzuti, P. Pires Rosa, K.V. Tenório, C.C. Gatto, M. Negri, G.A. Casagrande, K.M. Pires de Oliveira, Synthesis, structural characterization, and prospects for new cobalt (II) complexes with thiocarbamoyl-pyrazoline ligands as promising antifungal agents, J. Inorg. Biochem. 213 (2020) 111277.
[97] L. Serpas, R.R. Baum, A. McGhee, I. Nieto, K.L. Jernigan, M. Zeller, G.M. Ferrence, D.L. Tierney, E.T. Papish, Scorpionate-like" complexes that are held together by hydrogen bonds: crystallographic and spectroscopic studies of (3-NH(t-butyl)-5-methyl-pyrazole)nMX2 (M = Zn, Ni, Co, Mn; n = 3, 4; X = Cl, Br), Polyhedron 114 (2016) 62–71.